Mechanistic description of convective gas-liquid mass transfer in biotrickling filters using CFD modeling

Patricio A. Moreno-Casas[1], Felipe Scott[1], José Delpiano[1], José A. Abell[1], Francisco Caicedo [2], Raúl Muñoz [3], Alberto Vergara-Fernández[1]*

[1] Green Technology Research Group, Facultad de Ingeniería y Ciencias Aplicadas, Universidad de los Andes, Chile.

[2] Facultad de Ingeniería, Universidad Mariana, Colombia.

[3] Institute of Sustainable Processes, Universidad de Valladolid, España

*Corresponding author: A. Vergara-Fernández. Tel.+ 562 2618 1441. E-mail: aovergara@miuandes.cl.

Keywords: Biotrickling; CFD; K_La; Mass transfer; Micro-tomography; Modeling; OpenFOAM,

Abstract

The gas-liquid mass transfer coefficient is a key parameter to the design and operation of biotrickling filters that governs the transport rate of contaminants and oxygen from the gas phase to the liquid phase where pollutant biodegradation occurs. Mass transfer coefficients are typically estimated via experimental procedures to produce empirical correlations, which are only valid for the bioreactor configuration and range of operational conditions under investigation. In this work, a new method for the estimation of the gas-liquid mass transfer coefficient in biotrickling filters is presented. This novel

methodology couples a realistic description of the packing media (polyurethane foam without a biofilm) obtained using micro-tomography with computational fluid dynamics. The two-dimensional analysis reported in this study allowed capturing the mechanisms of the complex processes involved in the creeping porous air and water flow in the presence of capillary effects in biotrickling filters. Model predictions matched the experimental mass transfer coefficients (± 30%) under a wide range of operational conditions.

1 Introduction

Biotechnologies represent a cost-competitive and environmentally friendly alternative to conventional physical/chemical technologies for the treatment of malodorous, volatile organic compounds (VOCs), greenhouse gases and biogas [1]. Of them, biotrickling filtration has become increasingly popular in the past decade based on its low gas residence time of operation (15 to 40 seconds [1,2]) and the potential to control key environmental parameters for microbial growth such as temperature, pH, and the concentrations of nutrients and toxic inhibitory metabolites [3,4]. Biotrickling filters (BTF) are packed-bed units where the packing material promotes an effective gas-liquid contact while supporting biofilm growth due to a continuous supply of liquid medium [1]. Hence, the design of this technology relies on the accurate description of both microbial biofilm kinetics and gas-liquid-solid interactions [4]. However, while the kinetics of pollutant biodegradation in biofilms have been consistently studied, the hydrodynamics of gas and liquid circulation determining pollutant mass transfer in the packing material of BTF are still poorly understood [5,6]. In fact, gas-liquid mass transfer in this bioreactor configuration is typically characterized using empirical methodologies for the determination of the global volumetric mass transfer coefficient (K_La) based on simplified mathematical

models [7–9].The experimental estimation of the volumetric mass transfer coefficient in BTF, as reviewed by Estrada et al. [9], San Valero et al. [4], Dumont [10] and Dupnock and Deshusses [11], is performed using VOC concentration measurements in the gas and liquid phases and CO_2 absorption in caustic water as the main experimental techniques. Unfortunately, the aforementioned approaches do not provide insights regarding the liquid and gas distribution and channeling inside the packed column (wetted area, velocity and pressure profiles, preferential flows). Therefore, new and more powerful techniques are required to describe all complex phenomena determining the gas-liquid pollutant mass transport in BTF.

In this context, the recent advances in Computational Fluid Dynamics (CFD) along with the increase in computational power over the past decades, has enabled the use of this powerful modelling tool for the design of off-gas treatment biotechnologies, which represents a new application in this field [12]. In order to study the complex geometry of a porous matrix, 3D digital imaging such as computational tomography or micro-tomography (depending on the resolution needed) can be used to assess the flow dynamics and compute the parameters of interest. For instance, the combination of 3D imaging and CFD techniques can be employed to obtain pressures and velocities at the pore scale. The coupling of CFD and computational micro-tomography has been used in recent years to analyze the flow through porous media [13,14], thus allowing for the characterization of the flow at the microscale. To the best of our knowledge, these techniques have never been applied in biofiltration systems for air treatment. A recent work by Prades and co-workers applied a CFD approach by using a commercial code where biological reactions were coupled to flow equations in order to simulate the liquid velocities and oxygen consumption in a flat plate (rather than a porous support) biofilm bioreactor [12]. The latter

CFD simulation represented an important step forward towards the description of gas-liquid flow in porous media BTF.

The present work explores the potential of CFD for the description of the gas-liquid mass transport in an abiotic BTF (not inoculated with microorganisms) using O_2 as a model gas and a detailed description of the polyurethane foam (PUF) support system obtained using 3D micro-tomography. The predictions of this CFD modeling approach were compared with the volumetric mass transfer coefficients empirically determined in a 6 L BTF operated under multiple operational conditions typically encountered under industrial scale.

2 Materials and methods

2.1 Mathematical model

The effect of capillarity should be considered when assessing the flow of liquid and gas (two-phase flow) in a porous material with sufficiently small pores, since liquid meniscus attached to the porous material can impact the flow of both phases. This can be achieved by adding a term to the fluid linear momentum or Navier-Stokes (NS) equations and by applying the Volume of Fluids (VOF) technique [15]. The NS equations (Eq. 1) can be coupled to the continuity equation (Eq. 2) for each fluid (liquid and gas) to obtain the pressure and velocity fields, while the liquid-gas interphase can be tracked by using the transport equation for the volume fraction of the two phases (Eq. 3). Both fluids were considered to be Newtonian, incompressible, isothermal and immiscible [16].

$$\rho\left(\frac{\partial U}{\partial t} + U \cdot \nabla U\right) = -\nabla p + \rho g + \mu \nabla^2 U + F_s \quad (1)$$

$$\nabla \cdot U = 0 \quad (2)$$

$$\frac{\partial \alpha}{\partial t} + \nabla \cdot (\alpha U) + \nabla \cdot \left(\alpha(1-\alpha)U_c\right) = 0 \quad (3)$$

Where, ρ is the fluid density (kg m^{-3}), U is the velocity vector *(u, v, w)* for the *x, y,* and *z* directions (m s^{-1}), respectively, g is the acceleration of gravity (m s^{-2}), p represents the pressure vector in space (Pa), μ denotes the dynamic viscosity of the fluid (kg·m^{-1}·s^{-1}), the operator $\nabla = \left(\frac{\partial}{\partial x}, \frac{\partial}{\partial y}, \frac{\partial}{\partial z}\right)$, and F_S is the surface tension force (N·m^{-1}). The variable α is the VOF indication function, which can be defined as the quantity of liquid per unit volume at each computational cell (i.e., if $\alpha = 1$ the cell contains only liquid, if $\alpha = 0$ the cell contains only gas, else there will be a mixture of both phases). Finally, the last term in Eq. (3) is a mathematical expression required to avoid excessive numerical diffusion, where U_c represents the convenient velocity field to compress the gas-liquid interphase.

The above equations were solved in OpenFOAM, where solutions to Eqs. (1) and (2) were obtained by applying the well-known predictor-corrector technique PISO (Pressure-Implicit with Splitting of Operators) algorithm [17], while the mathematical tracking of the interphase was achieved by solving Eq. (3) discretized in the InterFoam solver [18].

2.1.1 *Determination of the volumetric mass transfer coefficient (K_La)*

The volumetric mass transfer coefficient, K_La (s^{-1} or h^{-1}), is the product of the mass transfer coefficient, K_L (m s^{-1}), and the specific surface area, a (m^2 m^{-3}), where the mass transfer occurs. The specific surface area is the ratio of the surface S (m^2) of contact between the two phases, or interfacial area, and the volume V (m^3) of the bioreactor [19]. Several theories are typically used to determine K_L: film theory, penetration theory, surface renewal theory and boundary layer theory [20–23]. However, only the boundary layer

theory takes into account the hydrodynamic characterization of the system and provides a more realistic interpretation of the mass transfer phenomena occurring at the boundary layer [24].

The concentration distribution of a species A, C_A, within the air boundary layer is a function of its location, $C_A = C_A(x,y)$ and its thickness, δ_m, and it also depends on the distance from the plate leading edge [24]. In this regard, the momentum diffusivity and the mass diffusivity play a key role in the overall mass transfer phenomena, which can be accounted for with the Schmidt number, Sc. Whenever the momentum diffusivity is larger than the mass diffusivity, Sc is larger than 1 [25] and $\delta/\delta_m = Sc^{1/3}$. Moreover, an expression for an average Sherwood number, Sh_{av}, can be developed by connecting the average plate Reynolds number, $Re_l = \rho V_\infty l/\mu$, ($V_\infty$, is the air free stream velocity, right above the end of the boundary layer) and an average Schmidt number, Sc_{av}, along a flat plate of length l [24]:

$$Sh_{av} = \frac{K_L l}{D_{AB}} = 0.664(Re_l)^{1/2}(Sc)^{1/3} \quad (4)$$

Where K_L is the average mass transfer coefficient along the plate length, l, and D_{AB} is the diffusion coefficient between fluids A and B (air and water, 2×10^{-9} m^2 s^{-1} [26]). Considering that $S_c = \nu/D_{AB}$, an expression for the computation of the mass transfer coefficient can be obtained.

$$K_L = 0.664(l)^{-1/2}(V_\infty)^{1/2}(\nu)^{-1/6}(D_{AB})^{2/3} \quad (5)$$

where ν is the kinematic viscosity of the gas phase (1.51×10^{-5} m^2 s^{-1} for air). In the present study, the flat plate stands for the liquid-gas interphase, which is not flat. However, it will be assumed to be nearly flat for computational purposes. The estimation

of the specific area per unit volume of reactor is deferred to section 3.2. All constants applied in this study assume a temperature of 22 °C in order to be able to compare numerical and experimental results.

2.2 Polyurethane foam packing 3D micro-tomography

In order to solve the NS equations, a detailed and realistic description of the boundary conditions at the fluid-solid interface is needed, which requires a highly resolved three-dimensional image of the porous media. Nowadays, it is possible to construct such image by using X-ray computed micro-tomography (μCT). In the present study, a SKYSCAN 1272 high resolution X-ray micro-tomography scanner from Bruker was used with a maximum resolution of 0.35 μm. Due to the high resolution needed to obtain images of the PUF support, a small sample of the PUF support of the cylindrical reactor was scanned in the μCT. The height, width and depth of the sample were 1.58 cm, 1.58 cm and 0.76 cm, respectively (Figure 1 A.). The 3D image was saved in stl (stereolithography) format, and later used in OpenFOAM.

A 2D slice of the original 3D digitalized image was used in the present study due to the high computational cost required to numerically solve the flow (see Figure 1). The 2D image used in the simulations was 1.58 cm × 1.58 cm. From the 2D image, a fine grid was generated in OpenFOAM in order to discretize the porous voids within the PUF, where the liquid (water) and gas (air) were allowed to flow. A sample of the 2D mesh is shown in Figure 1, where the void spaces indicate the presence of the foam, and the discretized surfaces show the areas where the water and air will flow in the *x*-*y* plane (where *y* is vertical). In order to find a sound grid resolution (number of cells) to simulate all the cases of interest in the present work, a grid independence analysis was carried out (see Figure S1 in the Supplementary Material).

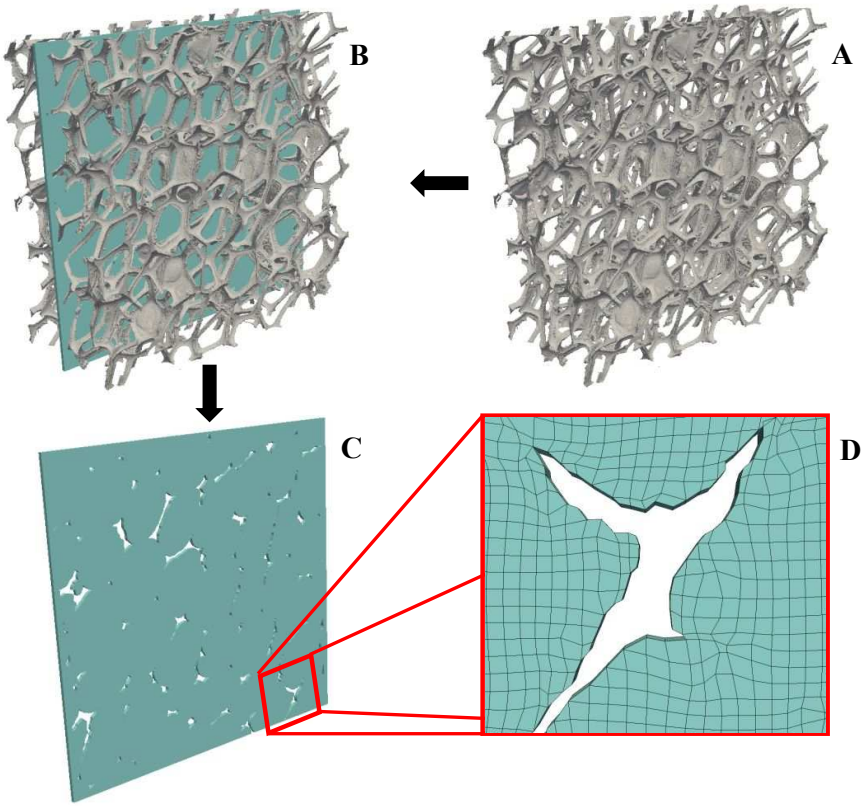

Figure 1. A) Digitalized PUF image using μCT. B) PUF image showing the computational domain (slice right at the PUF center). C) Computational domain used for simulations. D) Mesh zoom. White areas indicate the presence of PUF. Only PUF void areas were discretized.

Since the computational domain is much smaller than the complete BTF, the digitalized PUF was assumed to be far away from the BTF inlet and outlet, and far away from the column inner walls. In this way, the velocity conditions of the digitalized PUF at the top and bottom were maintained from the experimental setup, while on the sides, cyclic/periodic effects were used to mimic BTF operation (see Figure 2).. The results from each simulation were considered to be representative of the average behavior of the BTF, while wall effects (air and water flow interaction with the reactor inner walls) were assumed to be negligible. The velocity boundary conditions, for the 2D grid, were: left and right boundaries had a periodic condition; upper and lower boundaries were defined

by the inlet and outlet water and air velocities according to each case of study. Wherever there is PUF support, the condition was defined as non-slip or zero velocity condition. The initial conditions for velocity and pressure, for the air and water flows, were defined in accordance to each numerical trial, which in turn was connected to a particular experimental condition (see Table 1). The time step for all simulations was fixed at 0.001 s and data was also saved every 0.001 s. The air and water flow in the BTF occurred in the y-direction (vertical direction). Thus, water entered the biofilter from the top and moved downwards, while the air entered from the bottom of the biofilter and moved upwards. A zero-pressure gradient condition was imposed in the support, whereas for the right and left borders the boundary condition was set to cyclic/periodic. For the inlet and outlet boundaries, the pressure was computed according to the velocity at each boundary cell by applying a total pressure set to $p_0 = 0$, while as the velocity U changed, the pressure was adjusted as $p = p_0 + 0.5|U|^2$.

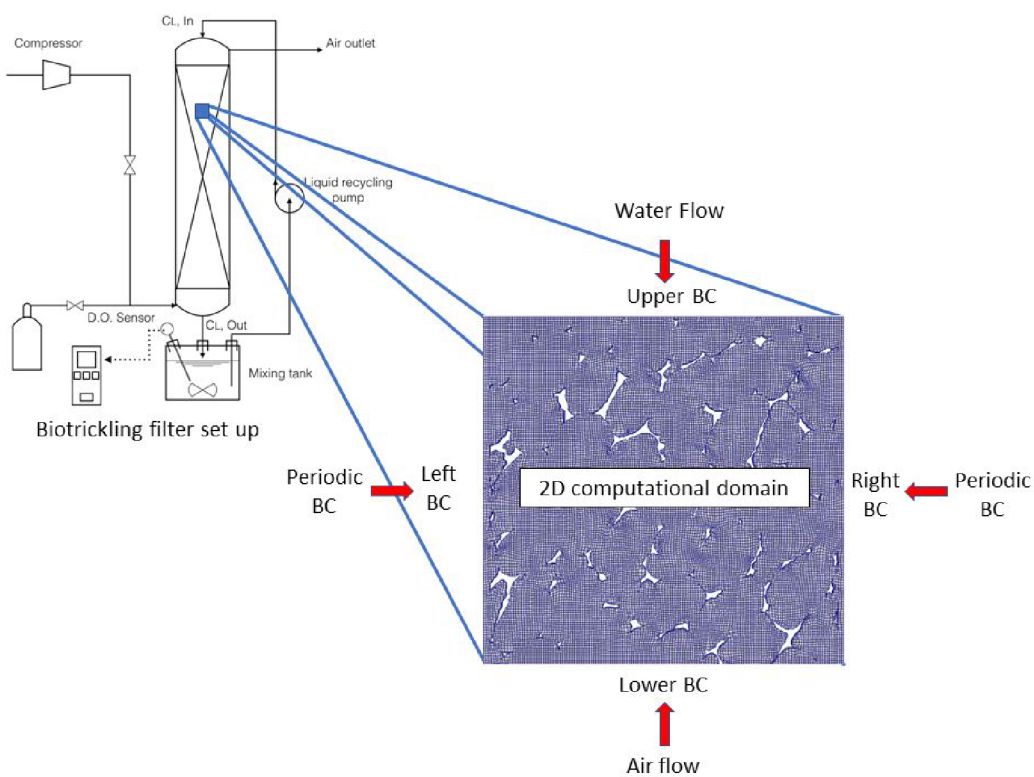

Figure 2. Schematization of the boundary conditions for the 2D microscale computational domain. BC stands for Boundary Conditions.

2.3 Experimental determination of the volumetric mass transfer coefficient in the BTF

The K_La values for O_2 were empirically determined in a 6 L polyvinyl chloride absorption column (0.08 m diameter × 1 m height) interconnected to a 1.5 L glass stirred tank reactor (magnetically stirred at 300 rpm). The absorption column was packed with a 4 L PUF cylinder, while the liquid level in the stirred tank was maintained at 1 L. The concentration of dissolved oxygen (DOC) was measured in the stirred tank reactor using a polarographic dissolved oxygen probe coupled to an O_2 transmitter 4100 (Mettler Toledo GmbH, Urdolf, Germany), which according to the manufacturer exhibited a response time of 90s to achieve 98% of the equilibrium concentration in a step change from an air saturated solution to an oxygen free aqueous solution at 25°C. Distilled water was used as a model liquid medium in the BTF to avoid any interference of the salt concentrations. A Watson Marlow 520 peristaltic pump was used to recycle the liquid medium from the stirred tank to the top of the absorption column, which was equipped with a cylindrical spray tubing (0.3 cm tip diameter × 10.5 cm length) located 4.5 cm above the PUF packed bed. Figure 2 and S2 (Supplementary Material B) illustrate a schematic of the experimental BTF and water irrigation system, respectively.

The volumetric gas-liquid mass transfer coefficients for O_2 were determined using the gassing-out method at empty bed gas residence times (EBRTs) of 17, 36, 60 and 240 s and liquid velocities of 2, 4, 11 and 17 m h^{-1} at each EBRT. The gassing-out method was selected due to its simplicity, the absence of dangerous chemicals and our previous expertise using it[9]. Prior to the determination of the K_La, the DOC in the recirculating

liquid medium was depleted with helium supplied from the bottom of the BTF counter-currently with the trickling liquid medium (at the corresponding liquid velocity and EBRT). Then, the helium stream was replaced with air at the target operational conditions and the DOC monitored to saturation. The empirical determinations of the K_La were conducted in duplicate at 22 ±1 ºC (controlled using a thermostatic water bath) using O_2 mass balances in the BTF and stirred tank reactor (Eq. 6 to 9), and the experimental data obtained in the test above described [8]. The abiotic BTF was modeled as 10 interconnected continuous stirred tank reactors (CSTRs) as follows:

$$\frac{dC^1_{L,out}}{dt} = (K_La)_{O_2}\left(\frac{C_G}{H} - C^1_{L,out}\right) + \frac{Q_L}{V_c}\left(C_{L,in} - C^1_{L,out}\right) \quad (6)$$

$$\frac{dC^j_{L,out}}{dt} = (K_La)_{O_2}\left(\frac{C_G}{H} - C^j_{L,out}\right) + \frac{Q_L}{V_c}\left(C^{j-1}_{L,out} - C^j_{L,out}\right), \text{j}=\{2,\ldots,9\} \quad (7)$$

$$\frac{dC^{10}_{L,out}}{dt} = (K_La)_{O_2}\left(\frac{C_G}{H} - C^{10}_{L,out}\right) + \frac{Q_L}{V_c}\left(C^{9}_{L,out} - C^{10}_{L,out}\right) \quad (8)$$

$$\frac{dC_{L,in}}{dt} = \frac{Q_L}{V_T}\left(C^{10}_{L,out} - C_{L,in}\right) \quad (9)$$

Where $C_{L,in}$ and $C^j_{L,out}$ stand for the dissolved O_2 concentration (g m^{-3}) at the inlet and outlet of each CSTR representing the absorption column (the first CSTR is at the top of the abiotic BTF); H is the Henry's law constant for O_2 (dimensionless), Q_L the recirculating liquid velocity (m^3 h^{-1}), V_C the packed bed volume (m^3) and V_T the volume of the stirred tank (m^3). In the estimation of K_La values in CSTRs it is necessary to account for the response time of the electrode when the response time of the probe is the same order of magnitude as $1/K_La$ [27]. This requirement arises since the delay in the electrode response produces a delayed dissolved oxygen concentration measurement and thus an underestimation of the K_La value [28]. However, in our system the concentration of

245 dissolved oxygen in the CSTR changes in small increments as oxygen rich water flowing
246 out of the abiotic BTF enters the CSTR where the electrode is positioned. Moreover, the
247 dynamic of flow circulation in the abiotic BTF and in the CSTR already introduced delays
248 that are accounted for in the model.

249 The kLa values for the 16 experiments shown in Table 1 were estimated by non-linear
250 fitting to the experimental data (in triplicate) to the model described by equations (Eq. 6
251 to 9) using the MATLAB's `nlinfit` function with default options. The 95% confidence
252 intervals for the estimated K_La values were calculated using MATLAB's `nlparci`
253 function. The comparison between model predictions and dissolved oxygen concentration
254 experimental data is provided in Supplementary Material.

255 **3 Results and discussion**

256 *3.1 Experimental mass transfer coefficients in a BTF with PUF as packing material.*

257 The experimental results obtained for K_La of oxygen dissolving into a trickling aqueous
258 solution under the 16 operational conditions tested are shown in Table 1. Higher values
259 of K_La were obtained at higher trickling medium velocities and lower EBRT's (i.e., higher
260 air velocities). From a fluid mechanics perspective, the water moving downwards due to
261 gravity interacts with the air moving upwards, causing shear at the water-air interface.
262 Hence, two mass transfer mechanisms may occur simultaneously: i) diffusion of O_2 into
263 water due to differences in O_2 concentration between the two phases, and ii) diffusion of
264 O_2 into water due to turbulence (momentum exchange) or shear between the moving
265 fluids at the interface. The magnitude of the shearing interaction between the two fluids
266 at the interface depends on the local Reynolds number of the fluid film in each section of
267 the wetted-column [24,29]. Hence, two boundary layers are formed: a concentration
268 boundary layer and a velocity or momentum boundary layer [24,25].

Table 1 Experimental K_La, and estimated K_L, a and K_La using CFD simulations, for the experimental conditions tested.

Operational condition	Water Velocity (m h^{-1})	EBRT (s)	Estimated a (m^{-1})	Estimated K_L (m h^{-1})	Experimental K_La (h^{-1}) [a]	Error in $C_{L,in}$ predictions (g m^{-3}) [b]
Case 1	2	240	233.59	0.476	112.58 ± 3.16	0.09
Case 2	4	240	190.53	0.700	144.04 ± 6.46	0.07
Case 3	11	240	180.35	0.693	125.16 ± 2.93	0.12
Case 4	17	240	227.42	0.699	156.60 ± 7.26	0.24
Case 5	2	60	223.82	0.567	122.29 ± 3.84	0.09
Case 6	4	60	215.07	0.675	112.13 ± 4.88	0.21
Case 7	11	60	205.19	0.748	167.86 ± 4.23	0.11
Case 8	17	60	193.27	0.688	167.21 ± 7.91	0.23
Case 9	2	36	234.54	0.579	173.39 ± 6.82	0.08
Case 10	4	36	141.97	0.832	183.68 ± 5.59	0.08
Case 11	11	36	218.09	0.742	232.89 ± 12.37	0.18
Case 12	17	36	209.07	0.905	259.24 ± 15.66	0.21
Case 13	2	17	190.72	0.696	189.28± 7.78	0.09
Case 14	4	17	150.05	1.009	212.50 ± 6.73	0.07
Case 15	11	17	210.37	1.062	249.60 ± 16.15	0.20
Case 16	17	17	208.76	1.154	380.87 ± 29.72	0.19

[a] Estimated K_La value from the experimental information and its 95% confidence interval.
[b] Average error calculated as the mean value of the absolute value differences between measured and predicted ($C_{L,in}$ in Eq. 9) dissolved oxygen concentrations.

Table 1 shows that the empirical K_La decreased by approximately 50% when the EBRT increased by a factor of 14, regardless of the trickling liquid velocity. On the other hand, the increase in K_La when the trickling liquid velocity increased from 2 to 17 m h^{-1} depended on the EBRT, with increases of 200%, 300%, 240% and 230% at EBRTs of 17, 36, 60, and 240 s, respectively. A similar behavior was reported by Lebrero et al. [8] and Estrada et al. [30] for toluene and methane K_La in BTF. Estrada et al.[31] reported K_La values for oxygen in the range 30–300 h^{-1} in an abiotic BTF with PUF as support, using liquid velocities between 0.5 and 5.0 m h^{-1} and EBRTs between 12 and 250 s.

3.2 Simulation of a 2D PUF slide of the biotrickling filter using CFD and comparison of predicted and experimental O_2 mass transfer coefficients.

A 2D CFD numerical simulation with a detailed description of the porous media was used in order to elucidate the physical mechanisms of O_2 gas-liquid mass transfer in a BTF at laboratory scale. 2D simulations were chosen over the 3D approach due to their model simplicity and the significant reduction in computational costs. Before all operational conditions were simulated, a sensitivity analysis for mesh independence was carried out (see Figure S1 in the Supplementary Material). The analysis of the computational results was based on steady-state conditions, which were reached with real time simulations of 10 s. In addition, it should be stressed that one of the main objectives of these simulations was to obtain a quantitative measure of the specific surface area where O_2 is dissolved into water, i.e., the gas-liquid interphase. Once the resulting distribution of the two phases was identified, the water-air interphase area (WAIA) was computed (see Figure S3 in the Supplementary Material).

The results obtained under steady state are shown in Figure 3. The simulation results are displayed in terms of the distribution of water, air, and air velocity vectors. The air velocity vector arrows graphically show the locations where preferential flow occurs as a result of the distribution of water patches. Preferential flow spots are likely to occur when two large patches of water separated by a small distance where air flows through are formed by the flow.

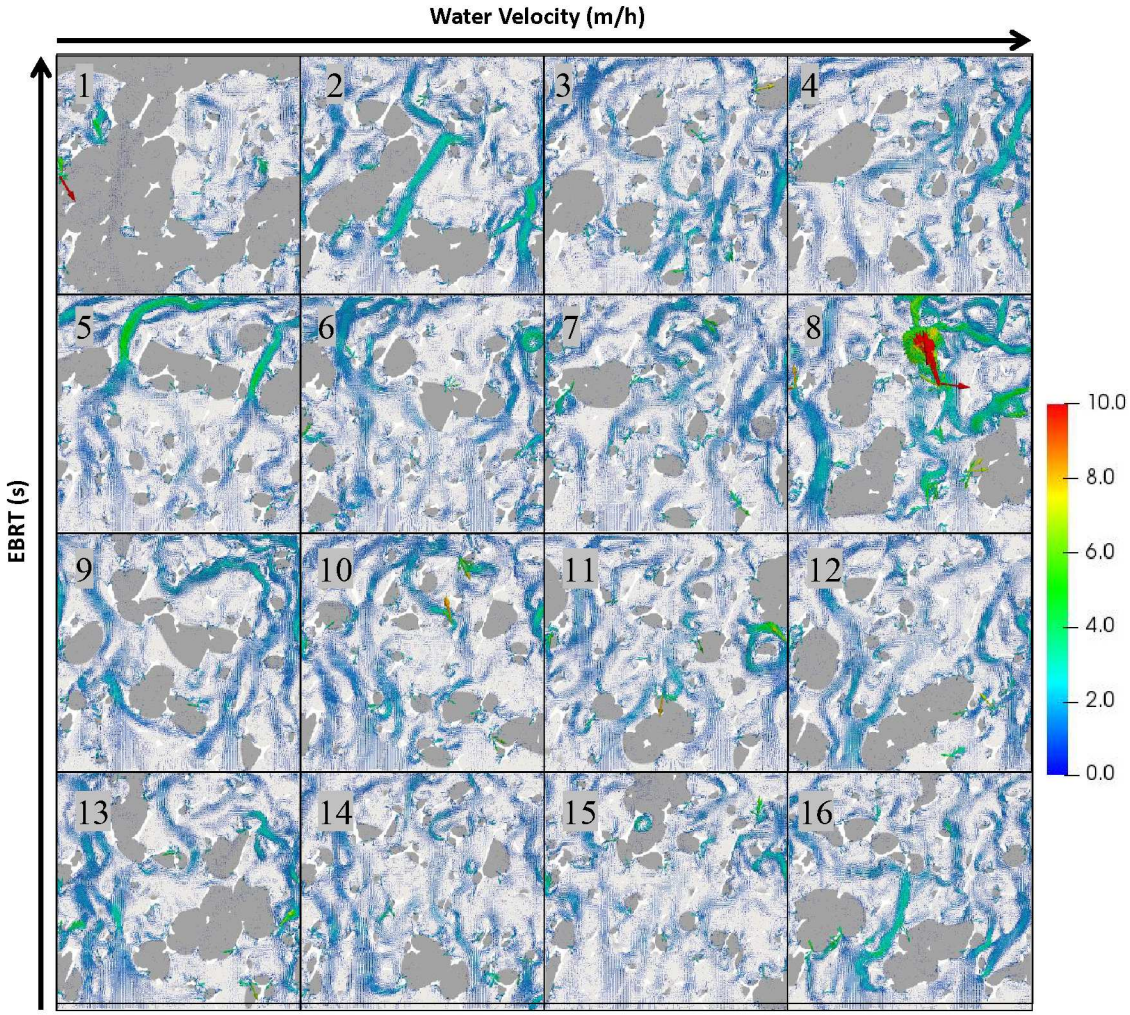

Figure 3. Water and air fraction results for the 2D PUF simulations. Dark grey color indicates the presence of water, light grey indicates the presence of air. White areas indicate the presence of PUF. Each row shows results for four different EBRT, from top to bottom: 240, 60, 36, and 17 s. Each column shows results for four different water velocities, from left to right: 2, 4, 11, and 17 m h^{-1}. Arrows indicate velocity vectors (m s^{-1}), with velocities values indicated in the colorbar. Cases are numerated from 1 to 16 in accordance with Table 1.

The numerical simulations conducted also showed that the volumetric mass transfer coefficient was greatly affected by the variations in EBRT and water velocity. As shown in Figure S4 (Supplementary Material), the variations in $K_L a$ were more significant at low EBRTs, i.e., changes in water feeding velocity greatly impacted the mass transport of oxygen into water at lower EBRT (higher air velocities). While at the highest EBRT analyzed (EBRT 240 (s)), the variations in water velocity exhibited a lower impact on $K_L a$. This can be explained by the increase of shear stresses near the water-air interphase, causing an increase in the O_2 mass transfer rate, a phenomenon that can be described using the boundary layer theory. This was represented in the numerical computations as an increase in the relative velocity difference between the water-air interphase and the free stream velocity of the air, V_∞.

The BTF water velocities directly impacted the diffusion of oxygen from the air into the trickling aqueous solution at the microscale level. The air free stream velocity (V_∞) gradually increased when increasing the trickling water velocity (see Figure S5 in the Supplementary Material) at EBRTs of 60, 36 and 17. According to Eq. (7), K_L increases as the square root of V_∞, and therefore, more oxygen is dissolved into water due to the increase of air flow momentum near the air-water interface. In addition, when the air flow as too low (EBRT 240), this variable did not affect the mass transport process. On the contrary, at low EBRT the variations in water velocities determined the distribution of water blobs, hence modifying the flow conditions of the air flow near each blob, and therefore changing V_∞.

The WAIA, the boundary layer and the velocities of air moving along the water-air interphase can be estimated using postprocessing (see Figure 4). Data from the cells

conforming such interface can be extracted from the simulation, as well as the location, length and area of the water-air interphase. From each cell conforming the air-water interface, a computational algorithm was used to estimate the air velocity of each cell above and perpendicular to the interface computational cells. When the air velocity remained constant, the boundary layer thickness position was identified (red dots in Figure 4), and the air free-stream velocity information was recorded and used to compute the average V_∞. At this point, all information for the computation of K_L was available (i.e. interface length, free-stream velocity, fluid kinematic viscosity and the air-water diffusion coefficient). Then, the average K_L for each segment of the air-water interface was computed. The diffusion coefficient of O_2 into water (2×10^{-9} m^2 s^{-1} [26]) at 22 ºC was used. In addition, the total WAIA for that case was divided by the computational domain volume (4.93×10^{-8} m^3) in order to obtain a (m^2 m^{-3}), which allowed the estimation of K_La. The K_La values estimated using CFD simulations for operational conditions 1 to 16 are shown in Table 1. The WAIA estimated from the simulations range from 142 to 235 m^2 m^{-3}. The WAIA did not strongly correlate to the improvement of K_La, but it does correlate with V_∞ (see figures S5 and S6 in the Supplementary Material). This suggests that under the operational conditions tested in this study, the enhancement in the air flow momentum near the WAIA played a key role in the increase the oxygen mass transfer in the BTF..

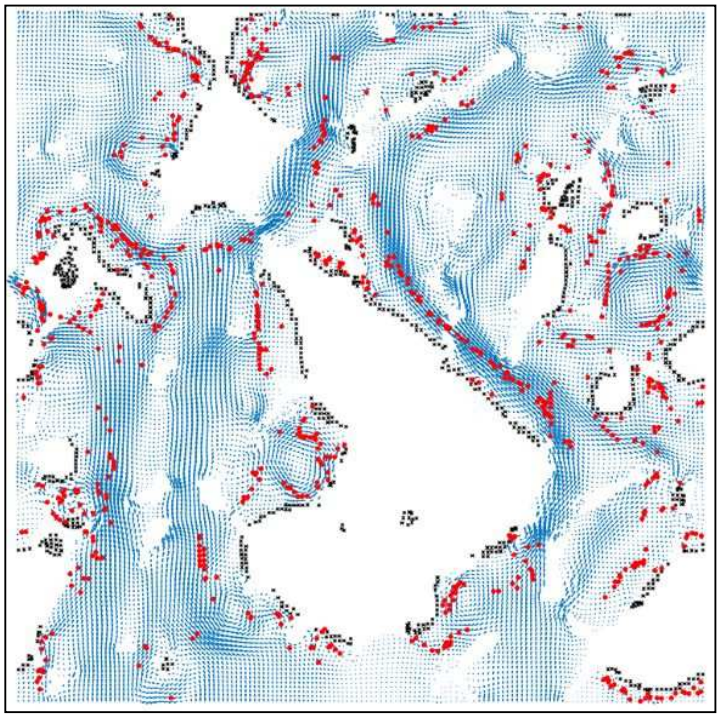

Figure 4. Graphical computation of the interfacial area, boundary layer thickness and air free stream velocity under steady state. The water-air interface is shown as black dots (one dot represents one computational cell). White patches indicate the presence of water. Red dots represent the boundary layer interface where the air free-stream velocity, V_{∞}, is reached. Blue arrows indicate air velocity vectors.

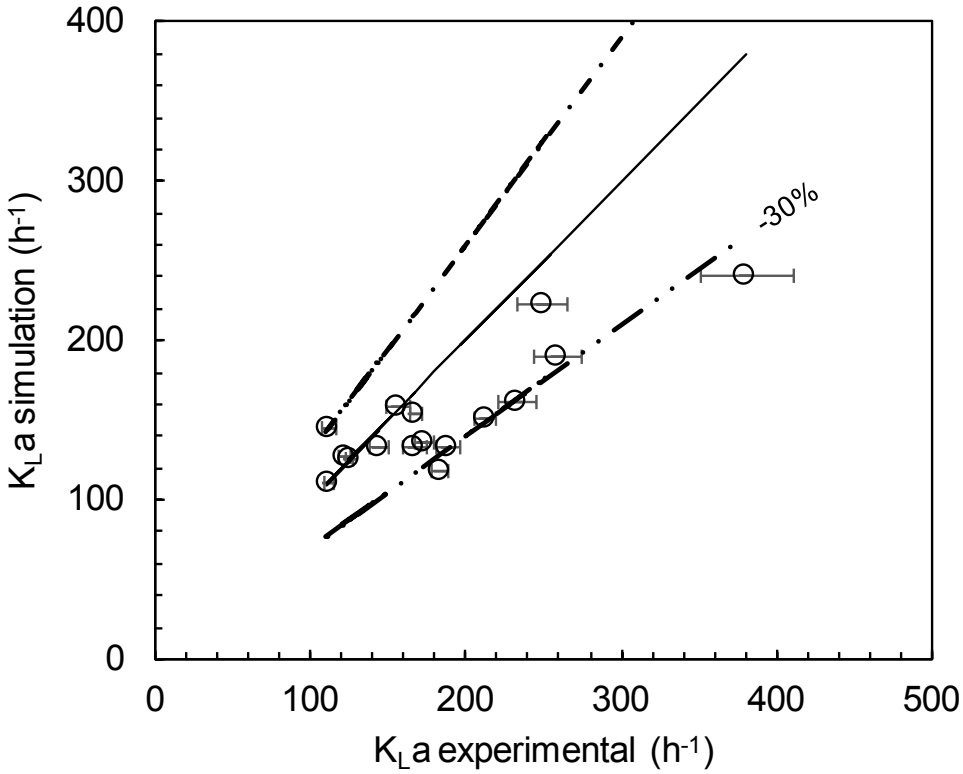

Figure 5. Comparison between simulated (Sim) and experimental (Exp) results of K_La. The diagonal broken lines limit the match between experimental and simulation results. The white circles show the actual simulated versus experimental results for the 16 operational conditions tested. Error bars represent the 95% confidence interval for the K_La values estimated from the experiments in Table 1.

The simulation results agree (within ± 30%) with the experimental values of K_La below 300 h^{-1} (Figure 5). Dorado et al.[32] determined the mass transfer coefficient for four packing materials, including PUF, and compared the results obtained with several literature correlations. None of the existing correlations provided an accurate description of the gas-liquid mass transfer coefficient for PUF. Among the correlations evaluated by Dorado et al.[32], the equation reported by Van Krevelen & Hoftijzer[33] and the correlation proposed by Kim and Deshussees[7] predicted mass transfer coefficients nearly one order

of magnitude lower than the experimental results. An attempt of fitting our experimental results using the constants and equations reported by Kim and Deshussees[7] and Van Krevelen & Hoftijzer[33], produced on average values representing only 23.5% and 18.9% of the experimental values, respectively. At this point it must be stressed that other correlations for the estimation of K_La in packed columns are typically not suitable in PUF-packed BTF since relevant parameters such as the packing equivalent diameter are not available.

The differences between the experimental and predicted K_La shown in Figure 5 may be due to the fact that this is a 2D micro simulation of a limited sample of PUF (0.0158 m × 0.0158 m). In addition, neither 3D nor wall effects (the latter entailing a local velocity reduction and channeling due to the presence of the column BTF inner wall) were considered in this simulation. At this point is should be also stressed that the boundary layer theory used to compute the average K_L values was capable of capturing the dynamics of the system. Other theories such us the film theory, penetration theory and surface renewal theory provided K_La values one or more orders of magnitude lower than their experimental counterparts, likely due to the fact that the latter techniques did not include the dynamic effects of the moving fluids (data not shown). The results here obtained highlighted the potential of the CFD modelling approach used to describe the volumetric mass transfer coefficients for different air and water flow conditions, despite all simplifications made in the simulations and the small computational domain used to mimic the operation of a 3D BTF column. A significant contribution of the present study to the field of gas treatment arises from the detailed description of the distribution of water patches formed due to the influence of surface tension in the PUF structure. The airflow in the BTF was not sufficient to overcome the water surface tension, even at the highest air velocities applied in the experimental and computational runs. However, the

combination of water moving downwards and air flowing upwards was capable of breaking the water "bubbles" down and help gravity to break the water patches into smaller ones. In this context, the presence of a large number of small patches of water creates a much larger air-water interphase than a large water patch containing the same amount of water. Similarly, a larger air-water interphase mediates a larger specific surface area for O_2 to dissolve into water, and therefore a higher $K_L a$.

Although more experimental validation and CFD model refinement are required to attain a realistic description of the system, the CFD modelling platform here developed allows obtaining key operational data at any point of the BTF. For instance, the determinations of the actual gas velocities inside the BTF column are very difficult to obtain experimentally without perturbing the natural flow patterns but could be easily recorded via CFD simulations. Similarly, the influence of key operational parameters on the interfacial area and free-stream velocities can be easily determined using this novel modelling approach.

Notation list

Symbol	Description	Units
$C_{L,in}$	dissolved O_2 concentration measured by the electrode	g m^{-3}
$C^{j}_{L,out}$	dissolved O_2 concentration of the jth CSTR in the BTF model	g m^{-3}
D_{AB}	diffusion coefficient of oxygen in water	m^2 s^{-1}
g	acceleration of gravity	m s^{-2}
H	Henry's law constant for O_2	-
$K_L a$	volumetric mass transfer coefficient	h^{-1}
Q_L	recirculating liquid flow	m^3 h^{-1}
p	pressure vector in space	Pa
Re_l	Reynolds number	-
Sc	Schmidt number	-
Sh	Sherwood number	-
U	Velocity vector	m s^{-1}
V_C	packed bed volume	m^3

V_T	stirred tank reactor volume	m^3
δ_m	boundary layer thickness	m
ρ	fluid density	kg m^{-3}
μ	dynamic viscosity of a fluid	$kg \cdot m^{-1} \cdot s^{-1}$
ν	kinematic viscosity of the gas phase	m^2 s^{-1}

Acknowledgements

The present work has been sponsored by CONICYT – Chile (National Commission for Scientific and Technological Research) project Fondecyt 1190521. The financial support from the Regional Government of Castilla y León is also gratefully acknowledged (UIC71 and CLU-2017-09).

J.D. thankfully acknowledges funding from projects Fondecyt 1180685, CONICYT Basal FB0008, and from Fondo de Ayuda a la Investigacion (FAI), Universidad de los Andes, INV-IN-2017-05.

References

(1) Estrada, J. .; Lebrero, R.; Quijano, G.; Kraakman, B.; R, M. Odour Abatement Technologies in WWTPs: Energy and Economic Efficiency. In *Sewage Treatment Plants: Economic Evaluation of Innovative Technologies for Energy Efficiency*; Tsagarakis, K., Stamatelatou, K., Eds.; IWA Publishing, 2015; pp 163–187.

(2) Cox, H. H. J.; Deshusses, M. A.; Converse, B. M.; Schroeder, E. D.; Iranpour, R. Odor and Volatile Organic Compound Treatment by Biotrickling Filters: Pilot-Scale Studies at Hyperion Treatment Plant. *Water Environ. Res.* **2002**, *74* (6), 557–563.

(3) Salamanca, D.; Dobslaw, D.; Engesser, K.-H. Removal of Cyclohexane Gaseous Emissions Using a Biotrickling Filter System. *Chemosphere* **2017**, *176*, 97–107.

https://doi.org/10.1016/j.chemosphere.2017.02.078.

(4) San-Valero, P.; Dorado, A. D.; Martínez-Soria, V.; Gabaldón, C. Biotrickling Filter Modeling for Styrene Abatement. Part 1: Model Development, Calibration and Validation on an Industrial Scale. *Chemosphere* **2018**, *191*, 1066–1074. https://doi.org/10.1016/j.chemosphere.2017.10.069.

(5) Moya, A.; Guimerà, X.; del Campo, F. J.; Prats-Alfonso, E.; Dorado, A. D.; Baeza, M.; Villa, R.; Gabriel, D.; Gamisans, X.; Gabriel, G. Biofilm Oxygen Profiling Using an Array of Microelectrodes on a Microfabricated Needle. *Procedia Eng.* **2014**, *87*, 256–259. https://doi.org/10.1016/j.proeng.2014.11.654.

(6) López, L. R.; Dorado, A. D.; Mora, M.; Gamisans, X.; Lafuente, J.; Gabriel, D. Modeling an Aerobic Biotrickling Filter for Biogas Desulfurization through a Multi-Step Oxidation Mechanism. *Chem. Eng. J.* **2016**, *294*, 447–457. https://doi.org/10.1016/j.cej.2016.03.013.

(7) Kim, S.; Deshusses, M. A. Determination of Mass Transfer Coefficients for Packing Materials Used in Biofilters and Biotrickling Filters for Air Pollution Control. 1. Experimental Results. *Chem. Eng. Sci.* **2008**, *63* (4), 841–855. https://doi.org/10.1016/j.ces.2007.10.011.

(8) Lebrero, R.; Estrada, J. M.; Muñoz, R.; Quijano, G. Toluene Mass Transfer Characterization in a Biotrickling Filter. *Biochem. Eng. J.* **2012**, *60*, 44–49. https://doi.org/10.1016/j.bej.2011.09.017.

(9) Estrada, J. M.; Dudek, A.; Muñoz, R.; Quijano, G. Fundamental Study on Gas-Liquid Mass Transfer in a Biotrickling Filter Packed with Polyurethane Foam. *J. Chem. Technol. Biotechnol.* **2014**, *89* (9), 1419–1424. https://doi.org/10.1002/jctb.4226.

(10) Dumont, É. Mass Transport Phenomena in Multiphasic Gas/Water/NAP Systems;

2019; pp 1–51. https://doi.org/10.1016/bs.ache.2018.12.001.

(11) Dupnock, T. L.; Deshusses, M. A. Detailed Investigations of Dissolved Hydrogen and Hydrogen Mass Transfer in a Biotrickling Filter for Upgrading Biogas. *Bioresour. Technol.* **2019**, *290*, 121780. https://doi.org/10.1016/j.biortech.2019.121780.

(12) Prades, L.; Dorado, A. D.; Climent, J.; Guimerà, X.; Chiva, S.; Gamisans, X. CFD Modeling of a Fixed-Bed Biofilm Reactor Coupling Hydrodynamics and Biokinetics. *Chem. Eng. J.* **2017**, *313*, 680–692. https://doi.org/10.1016/j.cej.2016.12.107.

(13) Soulaine, C.; Gjetvaj, F.; Garing, C.; Roman, S.; Russian, A.; Gouze, P.; Tchelepi, H. A. The Impact of Sub-Resolution Porosity of X-Ray Microtomography Images on the Permeability. *Transp. Porous Media* **2016**, *113* (1), 227–243. https://doi.org/10.1007/s11242-016-0690-2.

(14) Mirabolghasemi, M.; Prodanović, M.; DiCarlo, D.; Ji, H. Prediction of Empirical Properties Using Direct Pore-Scale Simulation of Straining through 3D Microtomography Images of Porous Media. *J. Hydrol.* **2015**, *529*, 768–778. https://doi.org/10.1016/j.jhydrol.2015.08.016.

(15) Hirt, C. .; Nichols, B. . Volume of Fluid (VOF) Method for the Dynamics of Free Boundaries. *J. Comput. Phys.* **1981**, *39* (1), 201–225. https://doi.org/10.1016/0021-9991(81)90145-5.

(16) Higuera, P.; Lara, J. L.; Losada, I. J. Three-Dimensional Interaction of Waves and Porous Coastal Structures Using OpenFOAM®. Part I: Formulation and Validation. *Coast. Eng.* **2014**, *83*, 243–258. https://doi.org/10.1016/j.coastaleng.2013.08.010.

(17) Versteeg, H. K.; Malalasekera, W. *An Introduction to Computational Fluid*

Dynamics: The Finite Volume Method, 2nd Ed.; 2009.

(18) Deshpande, S. S.; Anumolu, L.; Trujillo, M. F. Evaluating the Performance of the Two-Phase Flow Solver InterFoam. *Comput. Sci. Discov.* **2012**, *5* (1). https://doi.org/10.1088/1749-4699/5/1/014016.

(19) Painmanakul, P.; Wachirasak, J.; Jamnongwong, M.; Hebrard, G. Theoretical Prediction of Volumetric Mass Transfer Coefficient (KLa) for Designing an Aeration Tank. *Eng. J.* **2009**, *13* (3), 13–28. https://doi.org/10.4186/ej.2009.13.3.13.

(20) Murthy, Z. V. P.; Gupta, S. K. Estimation of Mass Transfer Coefficient Using a Combined Nonlinear Membrane Transport and Film Theory Model. *Desalination* **1997**, *109* (1), 39–49. https://doi.org/10.1016/S0011-9164(97)00051-9.

(21) Toor, H. L.; Marchello, J. M. Film-Penetration Model for Mass and Heat Transfer. *AIChE J.* **1958**, *4* (1), 97–101. https://doi.org/10.1002/aic.690040118.

(22) Asher, W. E.; Pankow, J. F. Prediction of Gas/Water Mass Transport Coefficients by a Surface Renewal Model. *Environ. Sci. Technol.* **1991**, *25* (7), 1294–1300. https://doi.org/10.1021/es00019a011.

(23) Carberry, J. J. A Boundary-Layer Model of Fluid-Particle Mass Transfer in Fixed Beds. *AIChE J.* **1960**, *6* (3), 460–463. https://doi.org/10.1002/aic.690060323.

(24) Dutta, B. K. *Principles of Mass Transfer and Separation Processes*; PHI Learning Pvt. Ltd., 2007.

(25) Bird, R. B.; Stewart, W. E.; Lightfoot, E. N. *Transport Phenomena*, 2nd ed.; Wiley, 2002.

(26) O'Brien, R. N.; Hyslop, W. F. A Laser Interferometric Study of the Diffusion of O 2 , N 2 , H 2 , and Ar into Water. *Can. J. Chem.* **1977**, *55* (8), 1415–1421. https://doi.org/10.1139/v77-196.

(27) Nielsen, D. R.; Daugulis, A. J.; McLellan, P. J. A Novel Method of Simulating Oxygen Mass Transfer in Two-Phase Partitioning Bioreactors. *Biotechnol. Bioeng.* **2003**, *83* (6), 735–742. https://doi.org/10.1002/bit.10721.

(28) Tribe, L. A.; Briens, C. L.; Margaritis, A. Determination of the Volumetric Mass Transfer Coefficient (KLa) Using the Dynamic Gas out-Gas in Method: Analysis of Errors Caused by Dissolved Oxygen Probes. *Biotechnol. Bioeng.* **1995**, *46* (4), 388–392. https://doi.org/10.1002/bit.260460412.

(29) Rohsennow, W. M.; Hartnett, J. P.; Cho, Y. I. *Handbook of Heat Transfer Fundamentals, 3rd Edition*; Prentie Hall, New Jersey, 1998.

(30) Estrada, J. M.; Lebrero, R.; Quijano, G.; Pérez, R.; Figueroa-González, I.; García-Encina, P. A.; Muñoz, R. Methane Abatement in a Gas-Recycling Biotrickling Filter: Evaluating Innovative Operational Strategies to Overcome Mass Transfer Limitations. *Chem. Eng. J.* **2014**, *253*, 385–393. https://doi.org/10.1016/j.cej.2014.05.053.

(31) Estrada, J. M.; Dudek, A.; Muñoz, R.; Quijano, G. Fundamental Study on Gas-Liquid Mass Transfer in a Biotrickling Filter Packed with Polyurethane Foam. *J. Chem. Technol. Biotechnol.* **2014**, *89* (9), 1419–1424. https://doi.org/10.1002/jctb.4226.

(32) Dorado, A. D.; Rodrí-guez, G.; Ribera, G.; Bonsfills, A.; Gabriel, D.; Lafuente, J.; Gamisans, X. Evaluation of Mass Transfer Coefficients in Biotrickling Filters: Experimental Determination and Comparison to Correlations. *Chem. Eng. Technol.* **2009**, *32* (12), 1941–1950. https://doi.org/10.1002/ceat.200900275.

(33) van Krevelen, D. W.; Hoftijzer, P. J. Studies of Gas Absorption. I. Liquid Film Resistance to Gas Absorption in Scrubbers. *Recl. des Trav. Chim. des Pays-Bas* **1947**, *66* (1), 49–65. https://doi.org/10.1002/recl.19470660106.